The Astrophysical Journal, 948:58 (9pp), 2023 May 1 https://doi.org/10.3847/1538-4357/acbef8

On the Energy-specific Photodissociation Pathways of $^{14}N_2$ and $^{14}N^{15}N$ Isotopomers to N Atoms of Different Reactivity: A Quantum Dynamical Perspective

Natalia Gelfand[1], Ksenia Komarova[1], Francoise Remacle[1,2], and Raphael D. Levine[1,3,4]

[1] The Fritz Haber Center for Molecular Dynamics and Institute of Chemistry, The Hebrew University of Jerusalem, Jerusalem 91904, Israel
natalia.gelfand@mail.huji.ac.il
[2] Theoretical Physical Chemistry, UR MolSys B6c, University of Liège, B4000 Liège, Belgium
[3] Department of Molecular and Medical Pharmacology, David Geffen School of Medicine, University of California, Los Angeles, CA 90095, USA
[4] Department of Chemistry and Biochemistry, University of California, Los Angeles, CA 90095, USA

Received 2022 December 22; revised 2023 February 5; accepted 2023 February 12; published 2023 May 5

Abstract

Photodissociation of the nitrogen molecule in the vacuum ultraviolet (VUV) is a major source of reactive nitrogen atoms in the upper atmosphere of Earth and throughout the solar system. Recent experimental studies have revealed strong energy dependence of the VUV photodissociation branching ratios to the $N(^4S_{3/2})+N(^2D_J)$ and $N(^4S_{3/2})+N(^2P_J)$ product channels, the primary dissociation pathways in the 108,000–116,000 cm^{-1} energy region. This produces $N(^2D_J)$ and $N(^2P_J)$ excited atoms that differ significantly in their chemical reactivity. The branching ratios oscillate with increase in the VUV excitation energy. We use high-level ab initio quantum chemistry to compute the potential curves of 17 electronic excited states and their nonadiabatic and spin–orbit couplings. The dynamics follow the sequential evolution from the optically excited but bound $^1\Sigma_u^+$ singlets. Spin–orbit coupling enables transfer to the dissociative triplet and quintet states. We compute the photodissociation yields through the dense manifold of electronic states leading to both exit channels. The dynamical simulations accurately capture the branching oscillations and enable a detailed look into the photodissociation mechanism. The major contribution to the dissociation is through the two lowest $^3\Pi_u$ states. However, for both isotopomers, at about 110,000 cm^{-1} there is an abnormally low dissociation rate into the $N(^4S_{3/2})+N(^2P_J)$ channel that enables comparable participation of triplet $^3\Sigma_u^-$ and quintet $^5\Pi_u$ electronic states. This leads to the first peak in the branching ratio. At higher energies, trapping of the population in the $3^3\Pi_u$ bound triplet state occurs. This favors dissociation to the lower-energy $N(^4S_{3/2})+N(^2D_J)$ channel and results in the observed second switch in branching ratios.

Unified Astronomy Thesaurus concepts: Cosmochemistry (331); Small molecules (2267); Ultraviolet spectroscopy (2284); Isotopic abundances (867); Reaction rates (2081); Theoretical models (2107); Photodissociation reactions (2266)

Supporting material: data behind figure

1. Introduction

State-to-state computational quantum dynamics that allow participation of multiple electronic states have been widely validated (Little & Tennyson 2013; Vrakking & Lepine 2019). One is thereby able to address processes of astrochemical importance (Thiemens & Lin 2021; Tychoniec 2021). This builds in an essential way on the progress in quantum chemistry (Werner et al. 2020) that provides not only accurate electronic potential energy curves but also their diverse couplings. Photodissociation is a central field of interest because it is a major source of reactive atoms in astrophysical environments. In the VUV energy region, the high density of excited electronic states makes for complex dissociation pathways, due to effective nonadiabatic coupling between different electronic states (Levine 2017, 2018). This leads to a nonmonotonic variation of the electronic character of the quantum state of the molecule as a function of its energy. The couplings reflect a large-scale breakdown of the Born–Oppenheimer separation of states that is useful at lower energies. The strong nonadiabatic couplings also make the character of the electronic state vary with internuclear distance. It is therefore no longer sufficient to use perturbative corrections; instead, a full, coupled electron and nuclear, dynamical approach is needed.

N_2 is a major constituent in the Earth's atmosphere and throughout the solar system and beyond. It has been widely studied for the understanding of solar photolysis in various regions of the galaxy, volatile chemistry, and prebiotic processes in the early solar system (Torr & Torr 1979; Strobel & Shemansky 1982; Meier 1991; Feldman et al. 2001; Balucani 2012; Dutuit et al. 2013; Fletcher et al. 2014; Thiemens & Lin 2021) and in the interstellar medium (Li et al. 2013). The N_2 molecule provides a clear example of the importance of the nonadiabatic couplings, as already evident from its optical absorption spectrum (Stahel et al. 1983; Spelsberg & Meyer 2001; Lewis et al. 2005, 2008). In regard to photodissociation, the lower-VUV optically accessible singlet states of N_2 are bound, but these states are isoenergetic with other electronic states that are dissociative. Highly resolved recent measurements of the branching fraction to different product channels (Song et al. 2016; Chang et al. 2019; Liu et al. 2021) supplement earlier studies (Walter et al. 1993).

Our dynamical computations demonstrate the interplay between different electronic states all the way to dissociation. N atoms of different electronic states and therefore of different reactivity (Donovan & Husain 1970; Suzuki et al. 1993; Herron 1999; Balucani 2012; Dutuit et al. 2013) are produced through a maze of crossings of electronic potential energy curves. Contrary to naïve expectations, this makes the experimentally observed energy dependence of the product states yield very nonmonotonic (Song et al. 2016; Chang et al. 2019; Liu et al. 2021). The recently measured state branchings for the two different isotopomers $^{14}N^{14}N$ (Song et al. 2016; Chang et al. 2019) and $^{14}N^{15}N$ (Liu et al. 2021) enable a critical test of the role of the mass-dependent nonadiabatic couplings.

High-level quantum chemistry plays several essential roles in any quantitative approach to reaction dynamics. First of all, the vibronic energy levels are very sensitive to the detailed potential energy curves, which are all highly anharmonic. In particular, for accounting for the role of the mass as revealed by the isotope effects in the vibronic energy levels, one needs a very accurate attractive part of the potential. Next, there is the spin–orbit coupling that enables efficient transfer between the stable singlets and the potentially dissociative manifold of triplet states. Due to the weak character of this spin–orbit coupling, the transfer between singlets and triplets is resonance sensitive (Lefebvre-Brion & Lewis 2007; Komarova et al. 2019). The triplet states are degenerate, and there are definite selection rules for the spin–orbit couplings of different magnetic sublevels, as spelled out in detail in Appendix A. Further on the route to dissociation, the triplet states are coupled by weak spin–orbit to the fivefold degenerate quintet states. That such states can be involved in the photodissociation and affect the branching was suggested by Song et al. (2016). For high-resolution spectroscopic studies of the quintets and corresponding theoretical analysis, see Carroll & Mulliken (1965), Partridge et al. (1988), Huber & Vervloet (1992), and Hochlaf et al. (2010).

Within a set of states of given symmetry, the strong nonadiabatic coupling makes the character of the electronic states highly dependent on the internuclear distance, and thus it is critical in the pathway to dissociation. Typically, this coupling is very localized in terms of the N–N bond length and therefore requires highly accurate computations. In other words, the crossings are characterized by a high value of the Landau–Zener nonadiabatic parameter (Levine & Bernstein 1974). The role of the different couplings varies nonmonotonically with the total excitation energy and therefore requires a close coupling dynamical computation.

The electronic states are dense but still discrete. The rapid change of electronic character with internuclear separation requires a quantal treatment also of the vibrational motion. We use a discretized variable representation of the N–N distance along a grid of localized nuclear basis functions (Lill et al. 1986; Light & Carrington 2000; Tannor 2007). The very localized nonadiabatic couplings require that we use a rather tight set of grid points. This small spacing of grid points allows the use of a finite difference approach to compute the matrix elements, diagonal and off-diagonal, of the momentum and of the kinetic energy (see Ajay et al. 2018, for more details).

Actual astrochemical experiments are complicated by the need to pay attention to the key role of shielding (Heays et al. 2014, 2017). However, this only makes the need for energy-resolved state-to-state data more pressing.

2. Energetics

Our purpose is to follow the coupled electron–vibration dynamics after a one-photon excitation from the ground state. This leads to a band of excited states at a narrow energy span. Essential details of the energetics and couplings that are needed in the discussion of the dynamics are shown in Figure 1 and in Appendix A. We focus attention on the region where both channels $N(^4S_{3/2})+N(^2D_J)$ and $N(^4S_{3/2})+N(^2P_J)$ contribute to the measured branching ratio (Song et al. 2016; Chang et al. 2019; Liu et al. 2021) as identified in Figure 1(a). Spectroscopic experiments show rotational line widths that are J dependent, mostly at higher values of J (Ubachs et al. 2001; Vieitez et al. 2007). The experimental results for the photodissociation branching use beams from a supersonic expansion and report only a quite moderate dependence on the rotational state. To understand the key features in the branching, it is sufficient that we compute dynamics for $J = 0$. The energy range is spanned primarily by the optically accessible singlet $^1\Sigma_u^+$ states. The Franck–Condon region is shaded in gray, indicating that these states can be effectively reached. The optically accessible singlet $^1\Pi_u$ states have a low Franck–Condon overlap in this energy range (Spelsberg & Meyer 2001) and hence are not shown. Figure 1(b) shows the triplet $^3\Pi_u$ and $^3\Sigma_u^-$ states that are coupled by spin–orbit coupling to the states of singlet character and thereby contribute to the photodissociation. In addition, there are quintet $^5\Pi_u$ states that are effectively coupled to the triplet $^3\Pi_u$ states via spin–orbit coupling. These states contribute to the dynamics, which we identify in the quantum dynamical computation for the full set of 17 excited singlet, triplet and quintet states, as shown in Appendix A.

Both panels (a) and (b) show the extensive role of avoided state crossings due to the nonadiabatic couplings, τ. The high magnitude of these terms is shown in panels (c) and (d), respectively. Note the steep character of these couplings as a function of the internuclear distance.

Adiabatic electronic states are stationary states of the electronic Hamiltonian when the nuclei are not allowed to move. Once the nuclei move, these states are coupled by nonadiabatic terms that are particularly important when the potential energies approach one another. In a situation like that shown in Figure 1, where the nonadiabatic terms are very localized, it is useful to think qualitatively in terms of a different set of states, typically called diabatic, where the chemical nature of the state is preserved. This is the case for repulsive triplet states as shown in Figure 1(b).

Dissociation into the lower-energy channel that produces $N(^2D_J)$ atoms is through the lowest-energy triplet $1^3\Pi_u$ state. It is largely populated from the higher-energy triplet states by the nonadiabatic coupling. The energetic path to dissociation that produces $N(^2P_J)$ atoms is more complex. There is a set of crossings that can be described as quintet and triplet repulsive channels. The second triplet potential, $2^3\Pi_u$, has a barrier at 112,000 cm^{-1}. It restricts dissociation at energies just above the threshold, 105,000 cm^{-1}. At these energies, the second quintet is repulsive and can be effectively coupled to the triplets. In addition, there is a repulsive $^3\Sigma_u^-$ state that is weakly coupled to the singlet states via spin–orbit coupling. Dissociation to the highest open channel, where both N atoms are excited, is above the energy range we discuss here.

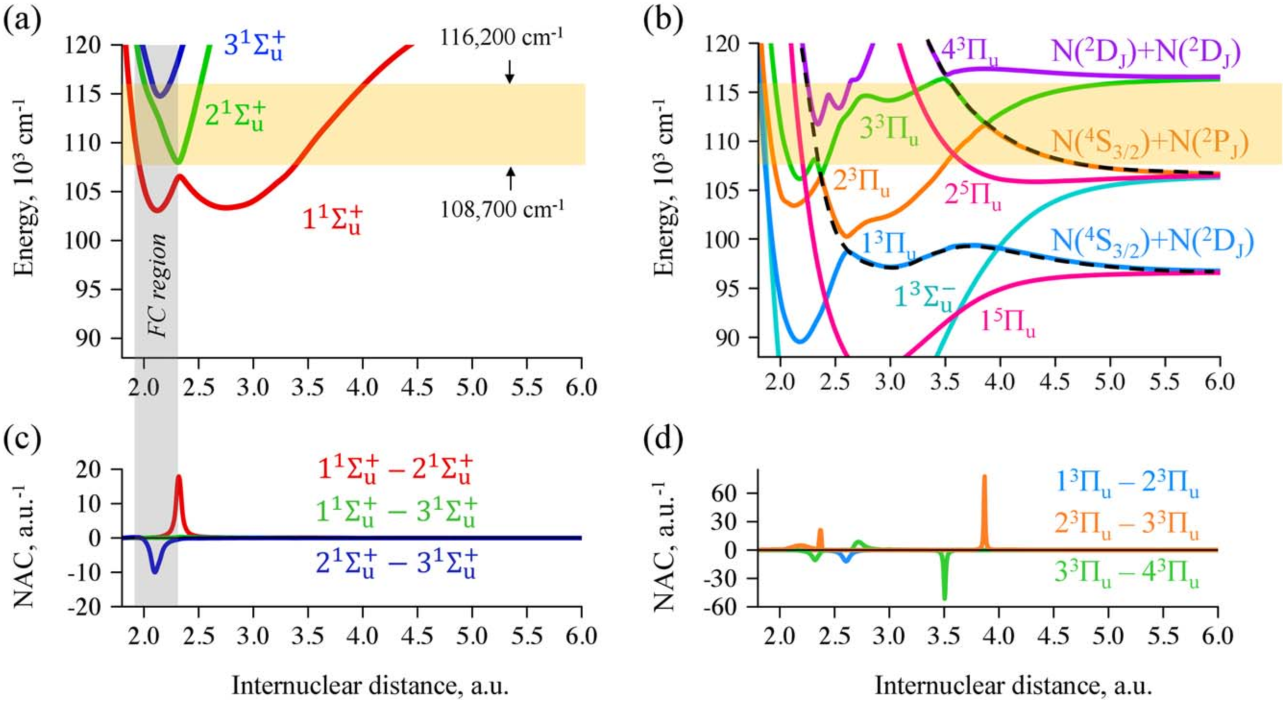

Figure 1. Potentials (a), (b) and nonadiabatic couplings, τ (c), (d), for the electronic states considered in the dynamics. There are three singlet $^1\Sigma_u^+$ states (a), one triplet $^3\Sigma_u^-$ and four triplet $^3\Pi_u$ states (b), each of which are triply degenerate, and two fivefold degenerate quintet $^5\Pi_u$ states (b). The spin–orbit coupling lifts the degeneracies. The adiabatic potentials are shown for all states shifted in energy scale by 850 cm^{-1}. For the triplet states, panel (b), the black dashed lines schematically depict the diabatic triplet repulsive potentials. The Franck–Condon (FC) region of high vibrational overlap with the ground electronic state is shaded in gray. The energy range of interest is here shaded in yellow.

(The data used to create this figure are available.)

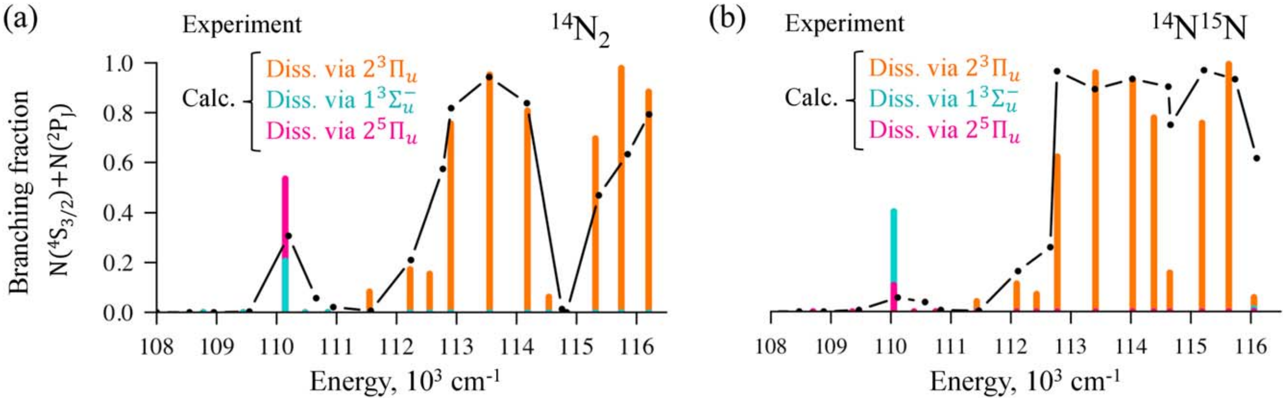

Figure 2. Comparison of the experimental (Song et al. 2016; Liu et al. 2021) (connected black points) and computational (in color) branching ratios into the N(^{4}S$_{3/2}$)+N(^{2}P$_J$) channel vs. the total energy for different isotopomers of nitrogen molecule: ^{14}N$_2$ (a) and ^{14}N^{15}N (b). The simulations do not resolve $J = 3/2$ and $5/2$. The color-coded columns resolve the computed branching fraction into the dissociation through the $2^3\Pi_u$ electronic state (shown in orange), that for the $^3\Sigma_u^-$ state (azure), and the contribution of the $2^5\Pi_u$ electronic state (magenta). The experimental data are taken for the lowest available rotational state excitation.

3. Dynamics

Numerically exact dynamical computations are performed separately, for a duration of 10 ps, for each of the optically accessible singlet $^1\Sigma_u^+$ vibrational states. These are the vibronic states that diagonalize the Hamiltonian of the singlet manifold. Nonadiabatic terms are included in this Hamiltonian, but the spin–orbit couplings are not. To ensure a narrow energy range, the light field is on for the first 3 ps; see Appendix B for more details. The short summary is that the nonmonotonic energy dependence of the branching ratios into the different channels matches the experimental results (Song et al. 2016; Liu et al. 2021) for both isotopomers. Figure 2 shows the branching ratio to the higher-energy channel. The corresponding branching fraction to the lower N(^{2}D$_J$) channel is shown in Figure 6 of Appendix C.

We emphasize that this agreement needs a very accurate quantum chemistry, and in particular, it is markedly sensitive to the signs of the nonadiabatic terms τ. These terms also mix the valence and the two Rydberg singlet $^1\Sigma_u^+$ states.

As an aid in the interpretation of nonmonotonic energy variation of the branching fraction, we computed the hitherto nonmeasured predissociation lifetimes of each excited vibrational $^1\Sigma_u^+$ singlet state. The predissociation lifetime is defined

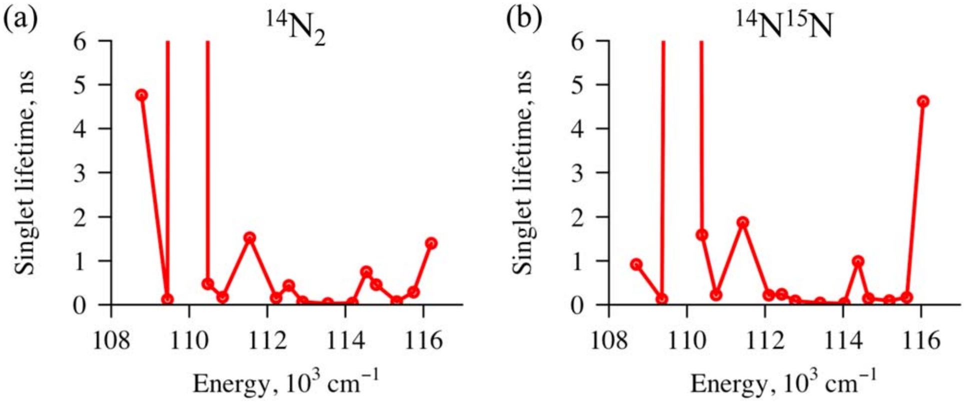

Figure 3. Predissociation lifetime computed for different $^1\Sigma_u^+$ vibrational quantum states in $^{14}N_2$ and $^{14}N^{15}N$ isotopomers of the nitrogen molecule. The lifetimes are given in Tables 2 and 3 of Appendix C. The very long predissociation lifetime at 110,144 cm^{-1} is estimated to be about 460 ns for $^{14}N_2$ and around 100 ns for $^{14}N^{15}N$.

as an inverse of the dissociation rate constant estimated from the decay of the population in all singlet electronic states during the 10 ps of the dynamics. This does not consider radiative processes, which typically occur on a longer timescale. The computed dissociation lifetime is not the total lifetime of a singlet state, but it allows us to qualitatively compare the dissociation rates for different singlet states.

The determined predissociation lifetimes for the unimolecular photodissociation are shown in Figure 3 and in Tables 2 and 3 in Appendix C. One singlet state, $^1\Sigma_u^+(\nu = 9)$, has a predissociation lifetime that is exceedingly high. This is consistent with an earlier report (Walter et al. 1993) of a very weak photofragment signal for low excited rotational states. For additional discussion, see Oertel et al. (1981) and Ubachs et al. (1993). Some of the other states also have predissociation lifetimes that vary by more than 1 order of magnitude. The shorter lifetimes are from those triplet energy bands that are purely repulsive.

The lowest energy range at which the branching ratio between the channels leading to $N(^2D_J)$ and $N(^2P_J)$ atoms becomes comparable is above 110,000 cm^{-1}. We see an extremely high predissociation lifetime for this energy (Figure 3), roughly 460 ns for $^{14}N_2$. The low overall rate of dissociation of this state makes the exit via the lowest triplet state to $N(^4S_{3/2})+N(^2D_J)$ channel comparable to the very slow dissociation coming from the triplet $^3\Sigma_u^-$ and quintet $^5\Pi_u$ states to $N(^4S_{3/2})+N(^2P_J)$; see Figure 2. Above 112,000 cm^{-1}, the effective coupling of the singlet and the repulsive triplet $^3\Pi_u$ states primarily favors the production of $N(^2P_J)$ atoms. At 114,500 cm^{-1}, trapping of the population in the high-lying bound triplet state, $3^3\Pi_u$, occurs. This state favors dissociation to the lowest $N(^4S_{3/2})+N(^2D_J)$ channel and results in the observed switch in branching ratios.

An additional interpretation of the dynamics is provided by Figure 4. It shows two shaded regions of low production of $N(^2P_J)$ atoms, Figures 4(a) and (b). Both are governed by barriers in the potentials of the triplet manifold. Singlet and triplet state populations for the dynamics in the case of the long-lived singlet state at the energy above 110,000 cm^{-1} are shown in Figure 4(c). The localized triplet states are primarily Rydberg in character. Throughout the energy range, those singlet states that are coupled to the triplet states of more Rydberg character live longer. The Rydberg triplet states are more localized in internuclear distance and hence have a lower overlap with valence singlet states that are delocalized; see Tables 2 and 3 in Appendix C. At higher energies, the increase in the branching to $N(^2P_J)$ is due to exit along the repulsive diabatic channel, as shown in Figure 4(d). Figure 4(e) shows the population trapping in the $3^3\Pi_u$ state at energies above 114,500 cm^{-1}, the second region of low production of $N(^2P_J)$ atoms.

Mass effects are important in isotope shifts of vibronic energy levels, as well as in the levels of $3^3\Pi_u$ quasibound trapped states as in the higher-energy band in Figure 4, at 114,538 cm^{-1}. Tunneling through the bottleneck barriers is also strongly mass dependent. Thus, there is a strong isotope effect for the photofragmentation at the excitation energies just below the barriers (Figure 4).

4. Concluding Remarks

4.1. Astrochemical Perspectives

Our results show that ab initio quantum dynamics through a complex landscape of coupled electrons and nuclei can help us interpret experimental observations of photodissociation of astrophysical importance. Crucial aspects are the strong nonadiabatic mixing of electronic states of the same symmetry and the selective spin–orbit coupling (Appendix A) of states of different symmetry. The example discussed is of a diatomic molecule, and the main limitation to additional applications is the number of vibrational modes, 3*N*-6 for the general case of an *N* atom polyatomic. The energetics provided by quantum chemistry sometimes need adjustments, but the primary challenge is obtaining the correct phase of the nonadiabatic couplings. The branching into different products is unexpectedly sensitive to this phase. Since there are dozens or more nonadiabatic events between the initially excited state and the products, this is a major concern. The spin–orbit intermultiplet coupling is weaker than the nonadiabatic intramultiplet coupling. Even so, a quintet state that is reached by a second order in the coupling does contribute, and so at higher energies there can also be septet states that may be populated as intermediate or final channels.

The different exit channels produce N atoms in different electronic states. These differ significantly in their chemical reactivity with other small molecules, such as H_2, CH_4, etc. (Donovan & Husain 1970; Suzuki et al. 1993; Herron 1999; Balucani 2012; Dutuit et al. 2013). Hence, the nonmonotonic variation in energy of the photodissociation branching may be imprinted onto the formation of more complex precursor

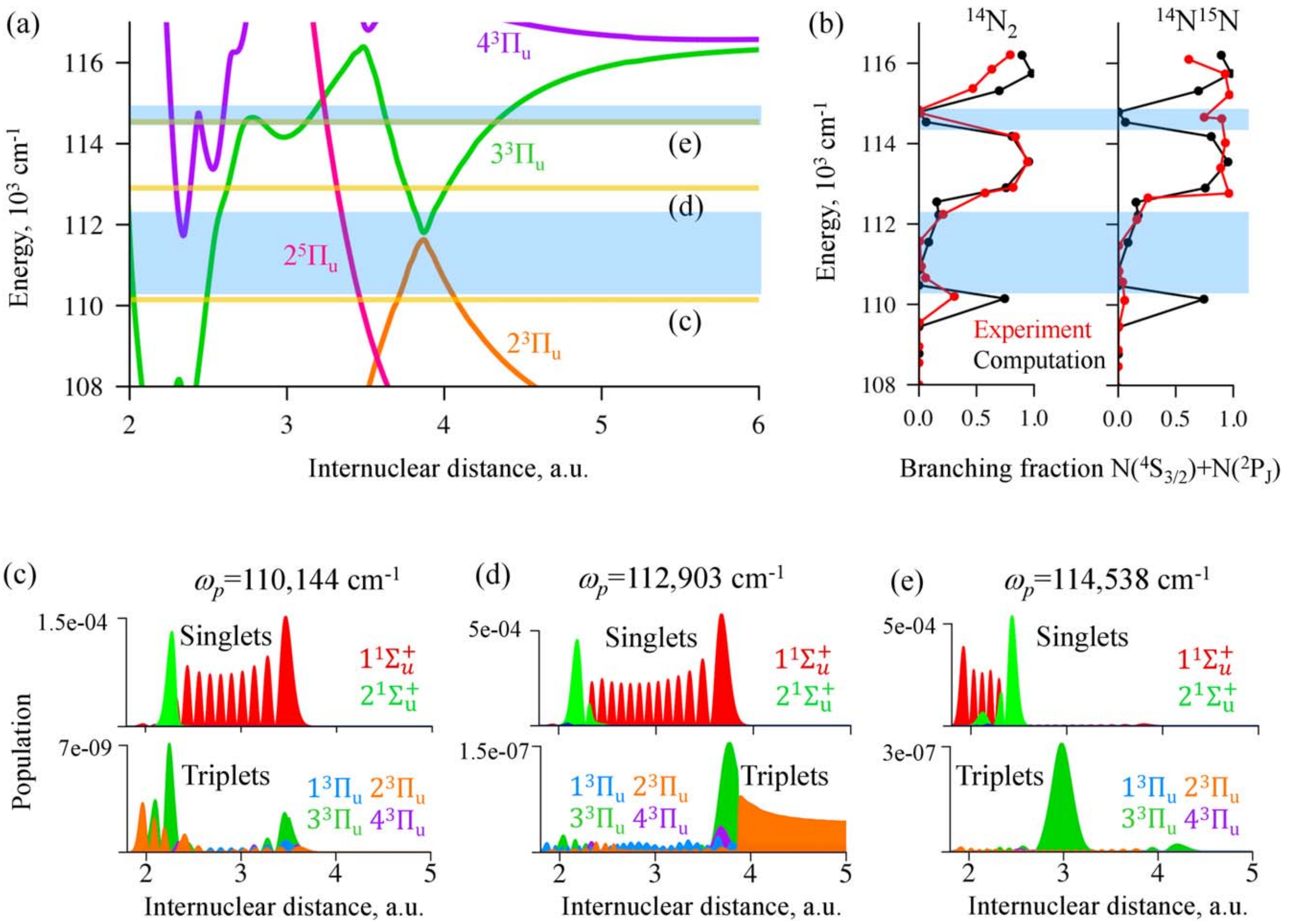

Figure 4. Toward understanding the regions of energy-sensitive branching. (a) Potential energy curves of the triplet and quintet electronic states and (b) the branching ratio into the $N(^4S_{3/2})+N(^2P_J)$ channel for $^{14}N_2$ and $^{14}N^{15}N$ isotopomers. These are the same results as shown in Figure 2. The two blue bands show regions of energy with low yield into this channel. The two bottom rows show results of quantum dynamical computations of dissociation in $^{14}N_2$ after 10 ps at three different excitation energies for singlet and triplet states. The electronic states are color coded, and the probabilities $|C_{nj}(t)|^2$ are shown as a function of the internuclear distance R grid point j for each electronic state n. Three different dynamical scenarios are shown that correspond to the energies identified in yellow in panel (a). (c) Slow rate of dissociation at the energy 110,144 cm^{-1}, leading to the first peak in the branching fractions vs. energy. A primarily valence-state singlet is only weakly coupled to a localized triplet state below the barrier in the $2^3\Pi_u$ potential. (d) Effective coupling to a repulsive triplet diabatic state at an energy slightly higher than in (a). (e) A triplet state trapped in a well in the $3^3\Pi_u$ potential, leading to a switch in the branching at this higher energy.

compounds of biological relevance in the solar system, as well as in other diverse environments, including the interstellar medium. The theory indicates that this nonmonotonic energy dependence is a manifestation of the many interacting potential energy curves. As such, it is expected to be rather general and exhibited in other molecules. Similarly the not-small isotope effect in the photodissociation branching is likely to be quite common.

4.2. Summary

A key characterization of the VUV photodissociation of N_2 is the nonmonotonic energy dependence of photofragmentation to $N(^4S_{3/2})+N(^2D_J)$ and $N(^4S_{3/2})+N(^2P_J)$ product channels leading to excited N atoms of different reactivity. In our simulation, the electronic excitation from the ground state is by a pulse of long duration—and thus narrow energy width—that is included in the dynamics. Optically excited bound singlet electronic states slowly transfer to the triplet dissociative states via weak spin–orbit interaction. Our simulations show longer predissociation lifetimes for the singlet states that are resonantly coupled to the Rydberg triplet states. In a particular case of a very slow singlet-to-triplet transfer, at about 110,000 cm^{-1}, the population exchange becomes comparable to the slow triplet-to-quintet transfer and is the origin of the lowest switch in the branching ratio. At a higher energy, we found two regions of low $N(^2P_J)$ atom production, in agreement with experimental data. In both cases, the trapping of the dissociation is observed due to barriers on the $^3\Pi_u$ highly anharmonic potentials on the way to the dissociation to $N(^4S_{3/2})+N(^2P_J)$ channel. A combination of quantum chemistry, high-level computations of potentials and couplings, and quantum dynamical simulation is essential in understanding the energy dependence of the photofragments' distribution.

We acknowledge financial support by the US–Israel grant No. 2019722 NSF–BSF Astronomy and Astrophysics. F.R. acknowledges the support of the Fonds National de la Recherche (F.R.S.-FNRS, Belgium), #T0205.20.

Appendix A

A.1. Details of Quantum Chemical Computations

The terms of electronic Hamiltonian: electronic potentials of singlet, triplet, and quintet electronic states, transition dipoles,

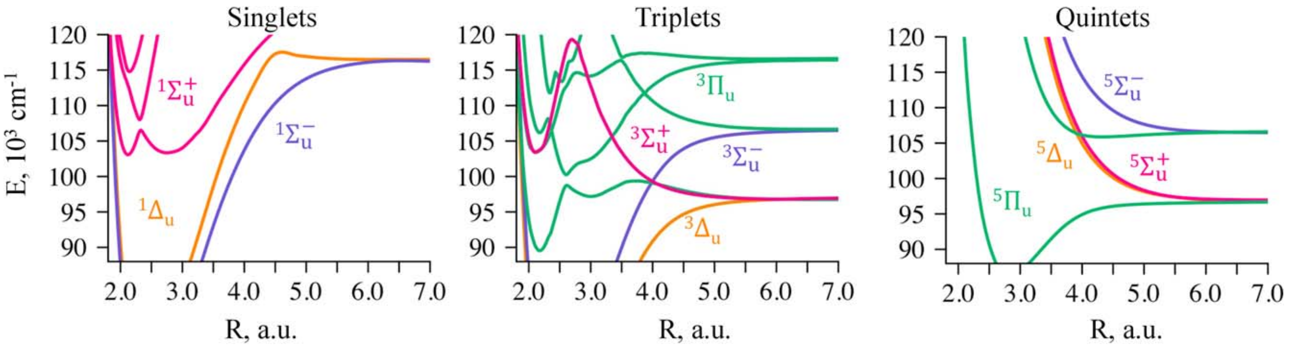

Figure 5. Potential energy curves of all 17 electronic excited states computed in the present work and included in the dynamics. Triplet and quintet electronic states are three- and fivefold degenerate, respectively.

Table 1
Spin–Orbit Selection Rules between the Singlet, Triplet, and Quintet Electronic States of Different Symmetries That Contribute Primarily to the Dynamics

	$^1\Sigma_u^+(m = 0)$				
$^1\Sigma_u^+(m = 0)$	0	$^3\Sigma_u^-(m = 0)$			
$^3\Sigma_u^-(m = 0)$	LSZ	0	$^3\Sigma_u^-(m = \pm 1)$		
$^3\Sigma_u^-(m = \pm 1)$	0	0	0	$^3\Pi_u(m = 0)$	
$^3\Pi_u(m = 0)$	0	0	LSX/LSY	0	$^3\Pi_u(m = \pm 1)$
$^3\Pi_u(m = \pm 1)$	LSX/LSY	LSX/LSY	0	0	LSZ
$^5\Pi_u(m = 0)$	0	0	LSX/LSY	LSZ	0
$^5\Pi_u(m = \pm 1)$	0	LSX/LSY	0	0	LSZ
$^5\Pi_u(m = \pm 2)$	0	0	LSX/LSY	0	0

Note. The notations (LSZ, etc.) are for the different spatial components of the spin–orbit coupling operator. *m* is the magnetic quantum number of the electronic state.

and nonadiabatic and spin–orbit couplings are calculated for each value of internuclear distance using a state-averaged, complete active space self-consistent field (CASSCF; Knowles & Werner 1985; Kreplin et al. 2019) approach followed by multireference configuration interaction (MRCI; Knowles & Werner 1988; Werner & Knowles 1988) calculations. The potential energy curves of all the computed electronic states are shown in Figure 5. In all computations, an active space of 17 orbitals ($4\sigma_u$, $3\sigma_g$, $4\pi_u$, $4\pi_g$, and $2\delta_g$) for 10 valence electrons is employed. The two lowest $1\sigma_u$ and $1\sigma_g$ orbitals are not included in the active space but are fully optimized in the CASSCF procedure. A restriction of only single occupancy for the higher Rydberg orbitals is used. We use a doubly augmented cc-pVQZ basis set with additional bond-centered *s* and *p* diffuse functions for a proper description of Rydberg and valence singlet and triplet states. All the quantum chemistry calculations are performed with the MOLPRO program package (Werner et al. 2020).

Triplet and quintet electronic states are degenerate states with different S_z projection ($m = -1$, 0, 1 for triplets and $m = -2$, -1, 0, 1, 2 for quintets). These states interact differently with singlet $^1\Sigma_u^+$ electronic states, as spin–orbit coupling integrals are subject to selection rules; see Table 1.

The potentials of the electronic states, transition dipoles, and nonadiabatic and spin–orbit couplings as a function of bond distance are available upon request to the authors.

Appendix B

B.1. Details of Quantum Dynamical Computations

We use the time-dependent Schrödinger equation of motion to compute quantum dynamics for the 17 excited and 1 ground electronic states of definite multiplicity; see Figure 5 of Appendix A. The equation of motion is defined for the amplitudes $C_{nj} = \Psi_n(R_j)$ at a given electronic state *n* and grid point *j* for the internuclear distance $R = R_j$. It is propagated in time via the Runge–Kutta method (Press et al. 1996). The interested reader should refer to Ajay et al. (2018) for more details. The nonadiabatic couplings $\tau_{nk}(R)$ between electronic states *n* and *k* are scaled by the finite difference momentum terms. We use the five-point finite difference method (Fornberg 1988) to compute the momentum and kinetic energy terms for the wave function defined on the grid. Spin–orbit coupling selection rules are detailed in Appendix A.

The interaction with the light field is governed by the transition dipole moment between the ground and excited singlet electronic states. An explicit time profile for the VUV light field is used. The duration of the pulse is set to be long enough to selectively excite specific vibrational levels of the singlet states, FWHM = 377fs. The carrier frequency is variable. It is tuned to selectively match the energies of the vibrational levels of the singlet states; see Tables 2 and 3 in Appendix C.

At large bond distances, $R > 6.2$ au, a complex absorbing potential is applied. The amount of population absorbed at long distances accumulated during 10 ps is used to define the relative branching ratio into the two channels. The predissociation lifetimes, shown in Figure 3, are defined as an inverse of the predissociation rate constants estimated by a linear fit for the logarithm of the time-dependent population in all the excited singlet states $|C_{nj}(t)|^2$, assuming a unimolecular exponential decay.

Appendix C

C.1. Results of the Quantum Dynamics

The results of the quantum dynamical simulations for branching ratios into the lower $N(^4S_{3/2})+N(^2D_j)$ channel are presented in Figure 6. Detailed information for each considered vibrational energy level is presented in Tables 2 and 3. The data in the tables correspond to the data plotted in Figures 2–4.

Table 2

Theoretical and Experimental (Song et al. 2016) Branching Ratios into the $N(^4S_{3/2})+N(^2P_J)$ Channel and Predissociation Lifetime for the $^{14}N_2$ Isotopomer

Energy, cm^{-1}	Singlet Character	Triplet Character	$N(^4S_{3/2})+N(^2P_J)$		Predissociation Lifetime, ns
			Computation	Experiment	
108778	Valence	Rydberg	0.000	0.000	4.76
109442	Valence	Valence	0.000	0.003	0.12
110144	Valence	Rydberg	0.745	0.307	(458.84)[a]
110476	Rydberg	Rydberg +Valence	0.000	0.057	0.47
110855	Valence	Rydberg +Valence	0.001	0.021	0.17
111549	Valence	Rydberg +Repulsive	0.084	0.006	1.54
112226	Valence	Rydberg +Repulsive	0.173	0.210	0.15
112551	Rydberg	Mixed	0.154	0.574	0.43
112903	Valence	Repulsive	0.757	0.818	0.06
113551	Valence	Repulsive	0.953	0.943	0.03
114182	Valence	Repulsive	0.810	0.838	0.04
114538	Rydberg	Bound $3^3\Pi_u$	0.062	0.013	0.54
114789	Valence	$3^3\Pi_u+4^3\Pi_u$	0.002	0.000	0.45
115315	Valence	$3^3\Pi_u+4^3\Pi_u$	0.697	0.468	0.07
115747	Valence	$3^3\Pi_u+4^3\Pi_u$	0.982	0.633	0.29
116202	Valence	$3^3\Pi_u+4^3\Pi_u$	0.895	0.793	1.41

Notes. The corresponding vibrational energy levels of the $^1\Sigma_u^+$ singlet electronic states are given in the first column. The experimental values are taken for the lowest available rotational state excitation.

[a] Estimated value.

Table 3

Theoretical and Experimental (Liu et al. 2021) Branching Ratios into the N($^4S_{3/2}$)+N(^2P_J) Channel and Predissociation Lifetime for the $^{14}N^{15}N$ Isotopomer

Energy, cm^{-1}	Singlet Character	Triplet Character	N($^4S_{3/2}$)+N(^2P_J)		Predissociation Lifetime, ns
			Computation	Experiment	
108702	Valence +Rydberg	Rydberg	0.000	0.000	0.95
109358	Valence	Rydberg	0.000	0.006	0.13
110049	Valence	Rydberg	0.510	0.056	(104.23)[a]
110385	Rydberg	Valence	0.000	0.038	0.58
110746	Valence	Rydberg+ Valence	0.000	0.006	0.22
111431	Valence	Rydberg +Repulsive	0.044	0.003	1.90
112097	Valence	Mixed	0.112	0.162	0.22
112428	Rydberg	Rydberg	0.070	0.258	0.24
112774	Valence	Repulsive	0.619	0.962	0.09
113410	Valence	Valence +Repulsive	0.948	0.890	0.04
114031	Valence	Repulsive	0.927	0.931	0.03
114385	Rydberg	Valence+ $3^3\Pi_u$+$4^3\Pi_u$	0.760	0.900	0.99
114649	Valence	$3^3\Pi_u$+$4^3\Pi_u$	0.153	0.747	0.14
115186	Valence	Valence+ $3^3\Pi_u$+$4^3\Pi_u$	0.750	0.966	0.09
115633	Valence	$3^3\Pi_u$+$4^3\Pi_u$	0.994	0.930	0.17
116052	Valence	$3^3\Pi_u$+$4^3\Pi_u$	0.115	0.613	4.74

Notes. The corresponding vibrational energy levels of the $^1\Sigma_u^+$ singlet electronic states are given in the first column. The experimental values are taken for the lowest available rotational state excitation.

[a] Estimated value.

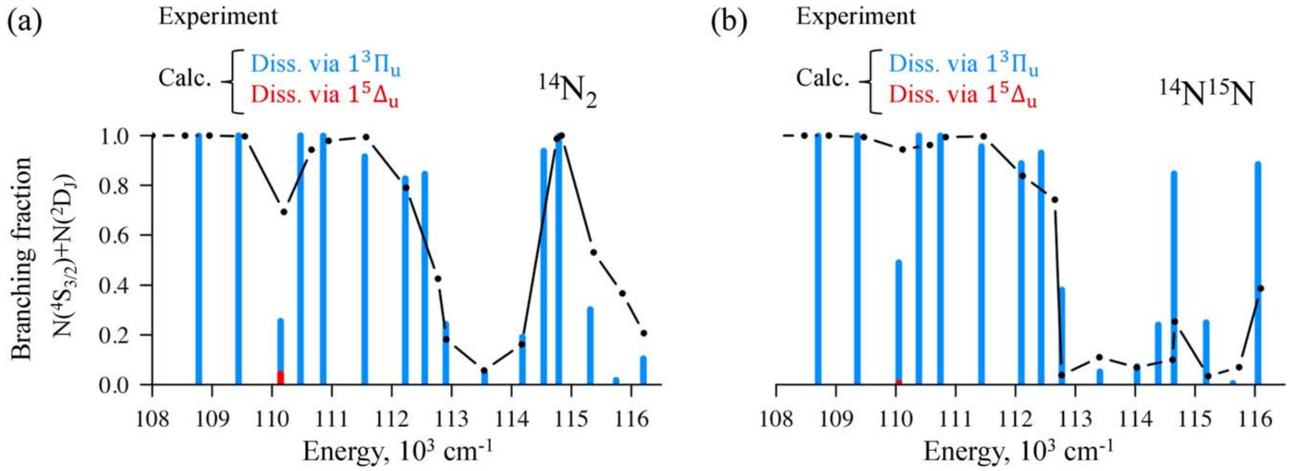

Figure 6. Comparison of the experimental (Song et al. 2016; Liu et al. 2021; connected black points) and computational (in color) branching ratios into the N($^4S_{3/2}$)+N(^2D_J) channel vs. the total energy for different isotopomers of nitrogen molecule: $^{14}N_2$ (a) and $^{14}N^{15}N$ (b). The experimental values are taken for the lowest available rotational state excitation.

ORCID iDs

Natalia Gelfand https://orcid.org/0000-0002-3034-0028
Ksenia Komarova https://orcid.org/0000-0001-6603-1377
Francoise Remacle https://orcid.org/0000-0001-7434-5245
Raphael D. Levine https://orcid.org/0000-0002-1973-8449

References

Ajay, J. S., Komarova, K. G., Van Den Wildenberg, S., Remacle, F., & Levine, R. D. 2018, in Attosecond Molecular Dynamics, ed. M. J. J. Vrakking & F. Lepine (Cambridge: The Royal Society of Chemistry), 308

Balucani, N. 2012, ChSRv, 41, 5473
Carroll, P. K., & Mulliken, R. S. 1965, JChPh, 43, 2170
Chang, Y. C., Liu, K., Kalogerakis, K. S., Ng, C. Y., & Jackson, W. M. 2019, JPCA, 123, 2289
Donovan, R. J., & Husain, D. 1970, ChRv, 70, 489
Dutuit, O., Carrasco, N., Thissen, R., et al. 2013, ApJS, 204, 20
Feldman, P. D., Sahnow, D. J., Kruk, J. W., Murphy, E. M., & Moos, H. W. 2001, JGR, 106, 8119
Fletcher, L. N., Greathouse, T. K., & Orton, G. S. 2014, Icar, 238, 170
Fornberg, B. 1988, Math. Comput., 51, 699
Heays, A. N., Bosman, A. D., & van Dishoeck, E. F. 2017, A&A, 602, A105
Heays, A. N., Visser, R., Gredel, R., et al. 2014, A&A, 562, A61
Herron, J. T. 1999, JPCRD, 28, 1453
Hochlaf, M., Ndome, H., & Hammoutène, D. 2010, JChPh, 132, 104310
Huber, K. P., & Vervloet, M. 1992, JMoSp, 153, 17
Knowles, P. J., & Werner, H.-J. 1985, CPL, 115, 259
Knowles, P. J., & Werner, H.-J. 1988, CPL, 145, 514
Komarova, K. G., Remacle, F., & Levine, R. D. 2019, JChPh, 151, 114308
Kreplin, D. A., Knowles, P. J., & Werner, H.-J. 2019, JChPh, 150, 194106
Lefebvre-Brion, H., & Lewis, B. R. 2007, MolPh, 105, 1625
Levine, R. D. 2017, PNAS, 114, 13594
Levine, R. D. 2018, ARPC, 69, 1
Levine, R. D., & Bernstein, R. B. 1974, Molecular Reaction Dynamics (New York: Oxford Univ. Press)
Lewis, B. R., Gibson, S. T., Sprengers, J. P., et al. 2005, JChPh, 123, 236101
Lewis, B. R., Heays, A. N., Gibson, S. T., Lefebvre-Brion, H., & Lefebvre, R. 2008, JChPh, 129, 164306
Li, X., Heays, A. N., Visser, R., et al. 2013, A&A, 555, A14
Light, J. C., & Carrington, T., Jr. 2000, in Discrete-Variable Representations and Their Utilization, ed. I. Prigogine & S. A. Rice (New York: Wiley), 263
Lill, J. V., Parker, G. A., & Light, J. C. 1986, JChPh, 85, 900
Little, D. A., & Tennyson, J. 2013, JPCB, 46, 145102
Liu, M., Jiang, P., Lu, L., et al. 2021, ApJ, 923, 196
Meier, R. R. 1991, SSRv, 58, 1
Oertel, H., Kratzat, M., Imschweiler, J., & Noll, T. 1981, CPL, 82, 552
Partridge, H., Langhoff, S. R., Bauschlicher, C. W., Jr., & Schwenke, D. W. 1988, JChPh, 88, 3174
Press, W. H., Teukolsky, S. A., Vetterling, W. T., & Flannery, B. P. 1996, Numerical Recipes in Fortran 77: The Art of Scientific Computing, Vol. 819 (2nd ed.; Cambridge: Cambridge Univ. Press)
Song, Y., Gao, H., Chung Chang, Y., et al. 2016, ApJ, 819, 23
Spelsberg, D., & Meyer, W. 2001, JChPh, 115, 6438
Stahel, D., Leoni, M., & Dressler, K. 1983, JChPh, 79, 2541
Strobel, D. F., & Shemansky, D. E. 1982, JGR, 87, 1361
Suzuki, T., Shihira, Y., Sato, T., Umemoto, H., & Tsunashima, S. 1993, J. Chem. Soc., Faraday Transactions, 89, 995
Tannor, D. J. 2007, Introduction to Quantum Mechanics: A Time-Dependent Perspective (Sausalito, CA: Univ. Science Books)
Thiemens, M. H., & Lin, M. 2021, in Triple Oxygen Isotope Geochemistry, ed. I. N. Bindeman & A. Pack (Berlin: de Gruyter & Co), 35
Torr, D. G., & Torr, M. R. 1979, JATP, 41, 797
Tychoniec, Ł., van Dihoeck, E. F., van't Hoff, M. L., et al. 2021, A&A, 655, A65
Ubachs, W., Eikema, K. S. E., & Hogervorst, W. 1993, ApPhB, 57, 411
Ubachs, W., Lang, R., Velchev, I., et al. 2001, CP, 270, 215
Vieitez, M. O., Ivanov, T. I., Sprengers, J. P., et al. 2007, MolPh, 105, 1543
Vrakking, M. J. J., & Lepine, F. 2019, Attosecond Molecular Dynamics (Cambridge: The Royal Society of Chemistry),
Walter, C. W., Cosby, P. C., & Helm, H. 1993, JChPh, 99, 3553
Werner, H.-J., & Knowles, P. J. 1988, JChPh, 89, 5803
Werner, H.-J., Knowles, P. J., Manby, F. R., et al. 2020, JChPh, 152, 144107